metals

MDPI

Article

Enhanced Mechanical Performance of SLM-Printed Inconel 718 Lattice Structures Through Heat Treatments

María J. Briones-Montemayor, Rigoberto Guzmán-Nogales, Parisa Majari, Jorge A. Estrada-Díaz, Alex Elías-Zúñiga, Daniel Olvera-Trejo *, Oscar Martínez-Romero * and Imperio A. Perales-Martínez

Tecnologico de Monterrey, Institute of Advanced Materials for Sustainable Manufacturing, Ave. Eugenio Garza Sada 2501, Col. Tecnológico, Monterrey 64700, N.L., Mexico; mj.briones@tec.mx (M.J.B.-M.); rigo.guzmann@tec.mx (R.G.-N.); majari@tec.mx (P.M.); j.estrada@tec.mx (J.A.E.-D.); aelias@tec.mx (A.E.-Z.); anel.perales@tec.mx (I.A.P.-M.)

* Correspondence: daniel.olvera.trejo@tec.mx (D.O.-T.); oscar.martinez@tec.mx (O.M.-R.)

Abstract: Selective laser melting (SLM) allows the production of complex lattice structures with tunable mechanical properties. This study proposes an integrated approach to enhance the mechanical properties of Inconel 718 (IN718) lightweight structures by applying distinct heat treatment protocols and tailoring key printing parameters. Four lattice geometries—body-centered cube (BCC), diamond, inverse woodpile (IWP), and gyroid—were selected for evaluation. Three heat treatment protocols were applied to assess their effect on mechanical behavior. Additionally, the influence of key SLM parameters such as laser power, scan speed, hatch spacing, and layer thickness on structural performance was investigated. By combining process tailoring and post-processing strategies, this work demonstrates a method to improve the mechanical response of complex IN718 lattices. The results highlight significant improvements in yield strength and energy absorption for high-performance applications in aerospace and automotive engineering.

Keywords: laser additive manufacturing; microstructure; heat treatments

check for updates

Academic Editor: Zhanyong Zhao

Received: 19 May 2025
Revised: 15 June 2025
Accepted: 15 June 2025
Published: 20 June 2025

Citation: Briones-Montemayor, M.J.; Guzmán-Nogales, R.; Majari, P.; Estrada-Díaz, J.A.; Elías-Zúñiga, A.; Olvera-Trejo, D.; Martínez-Romero, O.; Perales-Martínez, I.A. Enhanced Mechanical Performance of SLM-Printed Inconel 718 Lattice Structures Through Heat Treatments. *Metals* **2025**, *15*, 686. https://doi.org/10.3390/met15070686

Copyright: © 2025 by the authors. Licensee MDPI, Basel, Switzerland. This article is an open access article distributed under the terms and conditions of the Creative Commons Attribution (CC BY) license (https://creativecommons.org/licenses/by/4.0/).

1. Introduction

Selective laser melting (SLM) utilizes a high-power laser as the heat source to selectively fuse metal powder, enabling the production of intricate geometries that are often unattainable through conventional manufacturing methods, such as strut-based and triply periodic minimal surface (TPMS)-based lattice structures, in a layer-by-layer manner [1]. In this context, lattice structures refer to periodic, architected cellular geometries designed at the macroscale to enhance mechanical performance while reducing weight [2]. Their distinctive combination of low weight and enhanced mechanical efficiency has attracted significant attention [3,4].

Among the most studied lattice types are those based on TPMS geometries—smooth, continuous surfaces that efficiently distribute mechanical loads while minimizing stress concentrations. Representative TPMS lattices include the diamond, gyroid, and IWP (infinite periodic well-plate) structures. These architectures offer improved mechanical performance due to their inherent connectivity and curvature-driven design.

In addition to TPMS, body-centered cubic (BCC) lattices are frequently used due to their simple geometry and ease of fabrication. The BCC topology features structural elements converging at the center of the unit cell, promoting effective load distribution and stability under compressive forces. Together, these lattice types—diamond, gyroid, IWP,

and BCC—offer a range of mechanical properties and manufacturability, making them suitable candidates for applications in aerospace, automotive, and energy-absorbing systems.

The demanding operating environments in the aerospace, automotive, and biomedical industries, characterized by high mechanical loads, corrosive atmospheres, and elevated temperatures, require advanced materials with exceptional structural integrity. Inconel 718 (IN718), a nickel-based superalloy, has emerged as a preferred candidate due to its superior mechanical strength, corrosion resistance, and thermal stability. Notably, its compatibility with SLM processing mitigates issues such as cracking and elemental segregation, which are common limitations in the additive manufacturing of other high-performance alloys [5,6]. Recent developments have even demonstrated its feasibility in hybrid structures, such as IN718/Ti6Al4V combinations, enabling broader design flexibility for demanding applications [7].

SLM-fabricated IN718 lattice structures have thus shown significant promise in applications requiring energy absorption, mechanical strength, thermal efficiency, and environmental resistance. For instance, Zaharia et al. [8] developed low-mass, high-strength stiffening components using hyperbolic cell shapes, targeting aerospace applications. Banait et al. [9] linked microstructure and processing to improved energy absorption in IN718 lattices. Wang et al. [10] applied topology optimization for thermally stable IN718 components under unidirectional loads in aircraft, while Thuneman et al. [11] evidenced the corrosion resistance of SLMed IN718 for offshore applications.

Beyond SLM, other high-energy AM technologies have also enabled the fabrication of architected structures using different materials. Bai et al. [12] used selective laser sintering (SLS) to fabricate polyamide (PA2200) lattices with graded cell sizes, enhancing energy absorption. Ozdemir et al. [13] explored Ti6Al4V lattices fabricated via electron beam melting (EBM) under impact loading. Choi et al. [14] investigated hybrid stainless steel/IN718 structures fabricated using directed energy deposition (DED) on an SLM-built lattice, revealing unique interfacial bonding and crack propagation behavior.

The mechanical behavior of SLMed lattices is strongly influenced by the interplay between geometry, processing parameters, and post-processing treatments [1]. For example, Zhang et al. [15] demonstrated how high temperature exposure in SLMed Ti-6Al-4V structures could change the failure behavior from brittle to ductile. Similarly, Li et al. [16] reported that heat treatment protocols significantly affected the compressive response of $AlSi_{10}Mg$ lattices. Studies in SLMed IN718 have confirmed that tailored heat treatments can dramatically enhance mechanical performance. Yang et al. [5] and Wang et al. [17] reported improved strength and phase stabilization with optimized treatments at around 650 °C. Huang et al. [18] showed that multi-step heat treatments involving δ aging and precipitation aging refine microstructure, dissolve brittle phases, and promote the formation of strengthening γ' and γ'' phases, leading to enhanced isotropy and mechanical strength. Schneider et al. [19] further noted a non-linear correlation between heating cycles and tensile ductility in SLMed IN718.

Recent efforts have expanded toward understanding the role of heat treatments in IN718 SLMed lattice structures. For instance, Zaharia et al. [8] found that homogenization heat treatment significantly improved the microhardness and the compressive strength of IN718 lattices featuring spherical and hyperbolic designs. Banait et al. [9] reported that the undergone heat treatment of BCC IN718 lattices can induce a shift in deformation mode from bending-dominated to stretch-dominated when subjected to equivalent loads.

A comprehensive understanding of how varying heat treatment protocols influence lattice architectures remains underexplored. Although several studies have explored the post-processing of nickel-based superalloys fabricated by additive manufacturing, limitations remain regarding the correlation between heat treatment schedules, phase evolution,

and mechanical performance. For example, Zhang et al. [20] investigated the additively manufactured GH4099 superalloy followed by hot isostatic pressing (HIP) and subsequent heat treatments. Their results demonstrated that combining HIP and solution-aging treatments can yield tensile strengths (UTS) up to 1236 MPa and elongations of 25.5%, yet their approach focused primarily on recrystallization and long-period stacking-ordered (LPSO) phase formation rather than direct control of strengthening phase evolution in lattice-type geometries. Similarly, in the study by Ma and Wang [21], a nickel-based superalloy was SLM-printed, followed by a heat treatment that modified the grain orientation, increasing the yield strength and tensile strength of the material to 1362 MPa and 1410 MPa, respectively. However, their analysis concentrated on dislocation recovery and nano-precipitate formation in bulk samples, with limited insight into carbide suppression or the phase-specific contributions to mechanical enhancement.

In contrast, the present work systematically explores three distinct heat treatment schedules (HT1–HT3) applied to Inconel 718 lattice structures fabricated solely by SLM, without the use of HIP. By directly correlating optical microscopy, X-ray diffraction (XRD), and compression tests, this study provides a deeper understanding of phase transformations, particularly the suppression of detrimental δ and Laves phases, and the tailored precipitation of γ' and γ'' as a function of thermal cycles. This approach enables the optimization of mechanical properties through more accessible and scalable post-processing strategies.

This paper is structured as follows: Section 2 details the design and fabrication of four IN718 lattice geometries along with the application of three distinct heat treatment protocols to enhance yield strength and energy absorption. It also describes the experimental methodology, including compression testing under varying heat treatment conditions. Section 3 presents the numerical simulation approach using MATLAB R2019b (MathWorks, Nattick, MA, USA) PDE Toolbox to predict mechanical behavior. Section 4 discusses the results, analyzing force–displacement curves, microstructural changes, and the correlation between processing conditions and mechanical performance, while also validating the numerical model against experimental data. Finally, Section 5 summarizes the key findings.

2. Materials and Methods

2.1. Lattice Design

Lattice structures, also known as microporous solid structures [22,23], can be broadly categorized into strut-based, shell-based, and TPMS, each with distinct mechanical properties and potential applications [24]. The lattice geometries selected for this study include BCC, diamond, IWP, and gyroid, which were chosen for their potential in load-bearing and energy absorption applications. These structures, shown in Figure 1 with unit cell dimensions of 3 mm and 50% porosity, were designed according to the equations shown in Table 1.

Table 1 presents both the mathematical equations that define the studied lattice structures ($C = 0$, length of unit cell = 3 mm, number of cells = 4)—diamond, gyroid, BCC and IWP—and their geometric characteristics, i.e., volume, surface area, and volume/area ratio (V/A), alongside those of a cube ($L = 12$ mm) for comparative purposes. The intricate mathematical equations for each lattice lead to distinct volume-to-surface area ratios. For instance, the gyroid structure, having one of the lowest surface areas, exhibits the highest V/A ratio (0.394), whereas the BCC and IWP structures present higher surface areas and slightly lower V/A values, with the diamond structure presenting the lowest (0.329). In comparison, the solid cube shows a V/A ratio of 2 (with the significant values of volume and surface area of 1728 mm^3 and 864 mm^2, respectively), illustrating the significant increase in surface area introduced by the periodic lattice design. This information may help

to inform the design and optimization of SLM IN718 lattice structures, supporting the attainment of lightweight, high-performance components for aerospace, automotive, and other industries.

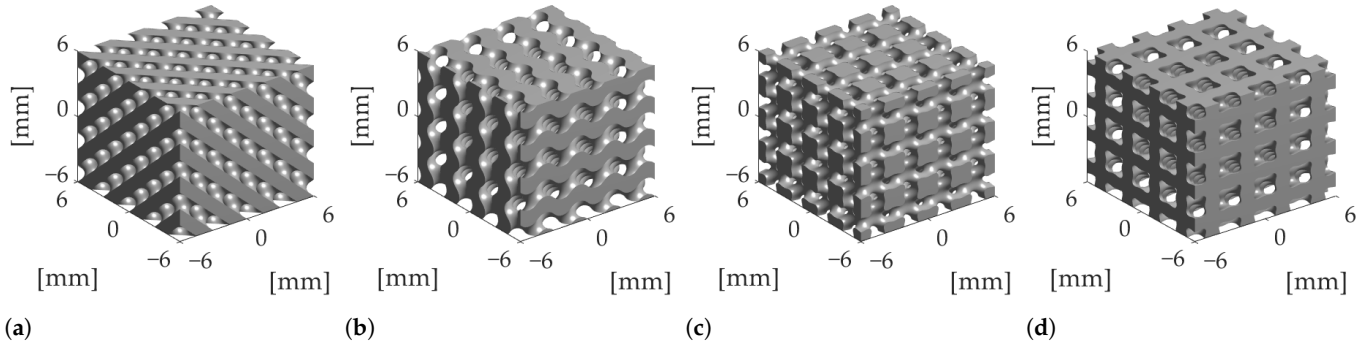


Figure 1. (**a**) Diamond, (**b**) gyroid, (**c**) BCC, and (**d**) IWP lattice structures ($C = 0$, length of unit cell = 3 mm, number of cells = 4), constructed with equations in Table 1.

Table 1. Mathematical equations, volume (V), surface area (A) and volume–area ratio (V/A) of the lattice structures ($C = 0$, length of unit cell = 3 mm, number of cells = 4) and the solid cube ($L = 12$ mm).

Lattice	Equation	V [mm^3]	A [mm^2]	V/A [mm]
Diamond	$\sin(x)\sin(y)\sin(z) + \sin(x)\cos(y)\cos(z) + \cos(x)\sin(y)\cos(z) + \cos(x)\cos(y)\sin(z) = C$	872	2644	0.33
Gyroid	$\cos(x)\sin(y) + \cos(y)\sin(z) + \cos(z)\sin(x) = C$	872	2213	0.39
BCC	$\cos(2x) + \cos(2y) + \cos(2z) - 2[\cos(x)\cos(y) + \cos(z)\cos(y) + \cos(x)\cos(z)] = C$	821	2364	0.35
IWP	$2[\cos(x)\cos(y) + \cos(y)\cos(z) + \cos(z)\cos(x)] - [\cos(2x) + \cos(2y) + \cos(2z)] = C$	923	2595	0.35
Cube	$x, y, z \in [0, L]$	1728	864	2.00

2.2. SLM IN718 Lattice Structures

The manufacturing of the lattice structures was conducted using a Renishaw AM 400 machine (Renishaw plc, Gloucestershire, UK) equipped with a pulsed-wave Nd-fiber laser with a maximum power of 400 W, a wavelength of 1075 nm, and a focus diameter of 75 µm. Argon gas flooded the building chamber to prevent oxidation during the SLM process while utilizing the reduced build volume (RBV) additament (Renishaw plc, Gloucestershire, UK). After spreading a homogeneous layer of metallic powder onto the build plate with the recoater blade, the laser beam selectively scanned the cross-sections of the lattice structures layer by layer until the parts were fully constructed. To analyze the influence of process parameters on the mechanical properties of SLM lattice structures and correlate them with microstructure, three energy density (E) values were selected, defined through Equation (1).

$$E = \frac{P}{v \times h \times lt} \tag{1}$$

P represents the laser power [W]; v is the scan speed [mm/s]; h is the hatch spacing [mm], i.e., the perpendicular distance between scanning lines; and lt is the layer thickness [mm]. The selected process parameters for this study are shown in Table 2. IN718 powder with a particle size between 15 and 45 µm was acquired from Renishaw (REN-IN718, Renishaw, Nuevo León, Mexico) for the manufacture of SLM lattice samples.

Experimental protocol P1 was determined as a derivation of the work of Estrada-Diaz et al. [25,26] and subsequent validation by Rosete [27]. In this work, a mathematical model for producing SLMed components with tailored densification by elucidating the complex interaction between process parameters and material properties was developed and experimentally validated. Through it, adequate levels of laser power and scan speed

can be tuned in order to achieve highly dense SLM parts. These processing conditions have been validated to result in IN718 SLM-printed components of 99.7% of relative bulk density [27]. Protocols P2 and P3 were selected through the energy density (E) concept to further explore the experimental landscape with E $\approx$ 46.3 J/mm^3 as a reference (noted in Table 2, now evaluating its effect on the mechanical properties exhibited by lattice structures).

Process parameters should be carefully selected considering the material properties, as highlighted by Estrada-Diaz et al. [28], ensuring the proper densification of the component while avoiding material evaporation/sublimation and dramatic thermal-induced residual stress caused by the excessive introduction of energy. In our study, heat treatment protocols are intended to help alleviate porosity concerns and help relieve thermal stresses, aiming to enhance the mechanical performance of IN718 SLM-printed lattice structure.

Table 2. Processing parameters for the SLM IN718 lattice structures.

	Parameter 1	**Parameter 2**	**Parameter 3**
Laser power, (P) [W]	300	300	200
Scan speed, (v) [mm/s]	900	1000	525
Hatch spacing, (h) [mm]	0.12	0.12	0.12
Energy density, (E) [J/mm^3]	46.3	41.7	52.9

2.3. Heat Treatments

Heat treatments are critical post-processing steps that play a key role on defining the mechanical properties and performance of SLM IN718 lattice structures. These treatments involve heating and cooling the material in controlled cycles designed to modify its microstructure, thereby enhancing properties such as strength, ductility, and toughness. The primary rationale for implementing tailored heat treatment protocols is to mitigate SLM effects (e.g., formation of non-equilibrium microstructures, high residual stresses, elemental segregation, and the development of undesirable phases such as Laves and intergranular carbides) and optimize the material's properties. Specifically, heat treatments are applied to relieve residual stresses, dissolve segregated phases, and promote the controlled precipitation of strengthening phases such as γ' and γ''. This process enhances microstructural homogeneity, stabilizes phase distribution, and restores or improves the mechanical behavior of the alloy. Thermal regimes involving different temperatures or durations influence the mechanical properties of IN718 lattice structures, the three heat treatment protocols employed in this study were selected based on their ability to promote microstructural homogenization, relieve residual stresses, and enhance phase precipitation without introducing excessive grain growth or oxidation. These protocols are grounded in prior literature and industrial standards that emphasize controlled phase evolution, particularly the dissolution of Laves and δ phases and the precipitation of strengthening γ'' and γ' phases [17,29].

In this study, three distinct post-processing heat treatments HT1, HT2, and HT3 were applied to IN718 samples produced via SLM, each designed to promote specific phase transformations and improve mechanical performance. HT1 consists of a step at 1065 °C, aimed at alleviating residual stresses induced by the high thermal gradients inherent to SLM. This step enables local diffusion and rearrangement of dislocations, contributing to microstructural stability. It is followed by a dissolution treatment at 1165 °C that dissolves undesirable secondary phases such as Laves, δ, and intergranular carbides, thereby enhancing chemical homogeneity. The subsequent double aging at 760 °C and 649 °C fosters the precipitation of γ'' (Ni_3Nb), the principal strengthening phase in IN718, along with minor formation of γ' ($Ni_3(Al,Ti)$), which adds thermal stability. The heat treatment protocol

for HT1 is illustrated in Figure 2a. The HT2 protocol (Figure 2b) includes a 2 h solution treatment at 1150 °C, succeeded by sequential aging treatments at 720 °C and 650 °C, for 8 and 6 h, respectively [17]. This controlled two-step aging process refines the morphology and distribution of γ'', enhancing the alloy's yield strength and hardness. HT3, by contrast, incorporates an initial high-temperature homogenization at 1170 °C and 1210 °C for extended durations, effectively dissolving segregation-prone phases and achieving a more uniform microstructure, Figure 2c. To stabilize the phase structure and maximize mechanical properties, a solution annealing at 940 °C is followed by a double aging at 720 °C and 621 °C [29]. Each heat treatment strategically leverages temperature-time regimes to direct the dissolution, formation, and controlled growth of critical strengthening phases in the alloy. Figure 2d presents a schematic representation of the phase transformations occurring in the lattice structures subjected to such thermal processing.

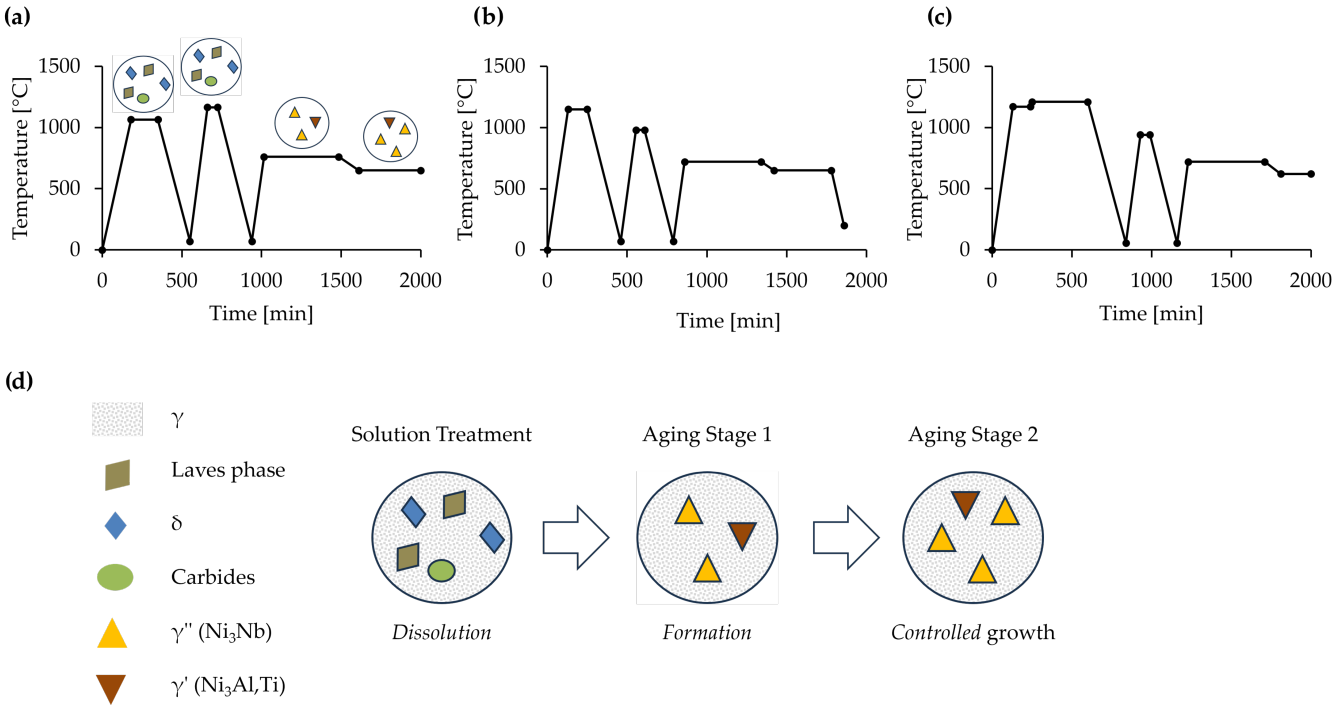


Figure 2. Temperature control programs for the selected heat treatments: (**a**) HT1, (**b**) HT2, (**c**) HT3, and (**d**) schematic representation of the phase transformations occurring in the samples subjected to the heat treatments.

The heat treatments were carried out in a GSL-1700X furnace (MTI Corporation, Richmond, CA, USA) capable of reaching a temperature of 1500 °C in an argon-filled chamber to prevent oxidation. The samples were placed in three labeled alumina containers (see Figure 3), which are needed for high temperatures. This setup ensured a uniform heat distribution and avoided contamination.

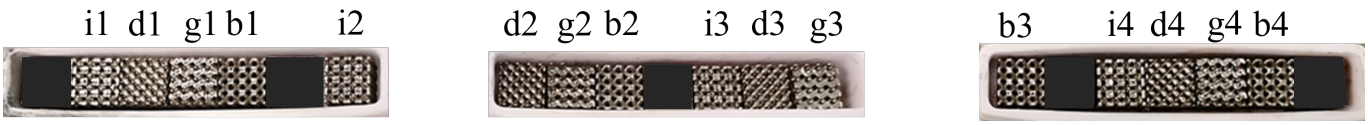


Figure 3. Lattices samples placed in alumina containers, IWP (i1, i2, i3, and i4), diamond (d1, d2, d3, and d4), gyroid (g1, g2, g3, and g4), and BCC (b1, b2, b3, and b4).

The effectiveness of these heat treatments was evaluated through a series of compression tests and microstructural analyses, as detailed in the following sections. Our findings

underscore the critical role of heat treatment protocols in tailoring the performance of SLM lattice structures, with each protocol providing unique advantages depending on the specific application or functional demands. The temperature control programs for the selected heat treatments are detailed in Figure 2. These programs outline the specific temperatures and durations employed in every thermal processing to achieve the desired microstructural changes and structural performance.

2.4. Mechanical Testing

The compression tests were conducted following the ISO 13314 [30] standard to evaluate the yield strength and energy absorption capabilities of the different lattices using a Shimadzu universal testing machine (AGS-X 250 kN, Shimadzu Co., Kyoto, Japan), equipped with a 250 kN load cell. For the testing conditions, a crosshead speed of 1 mm/s was selected, as it is the slowest available setting, ensuring accurate force measurements.

Each lattice structure was subjected to uniaxial compression until failure, with the load and displacement data recorded throughout the test. The yield strength was determined from the stress–strain curve, defined as the stress at which a permanent deformation of 0.2% strain occurs. Energy absorption was calculated by integrating the area under the stress-strain curve up to the point of failure, providing a measure of the material's ability to absorb and dissipate energy during deformation. Table 3 shows a summary of the mechanical properties of the SLM lattice structures after being treated by the heat treatments.

Table 3. Summary of yield strength and energy absorption for different lattice structures and heat treatments.

Heat Treatment	Lattice Structure	Yield Strength (MPa)	Energy Absorption (MJ/m³)
HT1	BCC	550	30
HT2	Diamond	600	35
HT3	IWP	650	40
HT2	Gyroid	700	45

The results of mechanical testing provide critical insight into the performance of the IN718 lattice structures subjected to distinct heat treatment strategies. Data on the attained yield strength and energy absorption can help identify the most effective heat treatment protocol to enhance its structural performance. In addition, compression tests help validate the effectiveness of heat treatments in relieving internal stresses and promoting the desired microstructural changes.

2.5. X-Ray Diffraction (XRD) Analysis

X-ray diffraction (XRD) analysis was conducted in a Mavern Panalytical (Worcestershire, UK) Empyrean machine to investigate the phase evolution in the as-built and heat-treated IN718 samples. The measurements were performed over a 2θ angular range of 15° to 80°, which covers the main diffraction peaks relevant to the γ matrix and strengthening phases of IN718. To improve the signal clarity, background noise was subtracted from the raw diffraction data. Phase identification was carried out using standard reference patterns from the Joint Committee on Powder Diffraction Standards (JCPDS) database. The resulting diffraction profiles were then analyzed to compare peak positions and intensities, enabling the assessment of phase stability and microstructural changes induced by the different heat treatment conditions.

3. Numerical Simulation of 3D-Printed Lattice Structures Using the PDE Toolbox

In this study, the finite element method (FEM) was employed via the Partial Differential Equation (PDE) Toolbox in MATLAB to model the complex geometries and boundary conditions of 3D-printed lattice structures and to predict their displacement under compressive forces. The PDE Toolbox offers robust capabilities and efficient computational performance for the numerical simulation of static compressive loads, making it well-suited for accurately capturing the mechanical behavior of intricate lattice designs. This simulation approach can be a practical procedure for evaluating the design of advanced lattice materials in high-performance applications where predictable deformation characteristics are challenging.

3.1. Estimation of Young's Modulus

The decision to numerically approximate the Young's modulus (or elastic modulus) of the printed material was driven by observed discrepancies between experimental data and numerical predictions when using elastic moduli calculated from 3D-printed compressive specimens or standard values reported in the literature [31,32]. These deviations can be attributed to manufacturing-induced microstructural variations, residual stresses, and the influence of complex geometries across multiple length scales inherent to the SLM process, such as the fractal characteristics noted in the powder bed that influence the densification behavior of SLMed components [26,33] and mechanical performance of polymeric lattice structures [34]. Moreover, conventional experimental methods, such as compression testing of solid specimens, frequently struggle to capture the elastic response of lattice structures, where geometric effects significantly alter mechanical behavior [35–37].

To address this variability, a parametric approach was implemented by evaluating a range of elastic modulus values from 2 to 200 GPa within the FEM simulations. This strategy allows the approximation of the elastic modulus of the additively manufactured IN718 when assessing structural performance, offering critical experimental-based insights into deformation behavior.

The simulation process began by importing lattice geometries from STL files generated (see Figure 1) according to the equations listed in Table 1. The material properties, including Young's modulus and Poisson's ratio, were defined, followed by the application of fixed boundary conditions and prescribed displacements on selected faces. A mesh is a key step in the simulation process, which defines the quality of the results. This was generated using the *generateMesh* function, which could require significant computational resources depending on the complexity of the geometries. The structural problem was then solved using the *solve* function to compute displacement fields and reaction forces. Relevant data, including maximum and minimum displacements, stresses, and reaction forces, were computed and analyzed.

A parametric study was conducted by iterating both Young's modulus values and displacement boundary conditions (ranging from 0.3 mm to 0.8 mm). For each iteration, the material properties and boundary conditions were updated, followed by mesh generation and problem solving to evaluate the mechanical response under varying conditions. When altering printing parameters in SLM, the Young's modulus of the printed samples can be significantly affected. Factors such as laser power, scan speed, hatch spacing, and layer thickness can influence grain size, porosity, and phase distribution within the IN718 lattice structures, closely related to mechanical properties, including Young's modulus. To account for this variability, a range of Young's modulus values was tested during simulations, generating force–displacement curves for each one. After printing the samples, compression tests were conducted to obtain experimental force–displacement data, which were then

compared with simulated curves to estimate the Young's modulus that most accurately reflects the mechanical behavior of the printed structures. By analyzing discrepancies between the experimental and simulated responses, the approximated Young's modulus of the printed IN718 can be inferred. In this comparison, it is important to keep the Young's modulus constant across all lattice geometries. This approach ensures that any variations in the force–displacement behavior are attributed solely to the geometry of the lattice structures, thereby isolating the influence of architecture from the material's intrinsic elastic properties.

3.2. Simulation and Experimental Validation Results

Four samples of each lattice geometry were fabricated and subjected to compression tests to obtain force–displacement data. The combination of numerical simulation and experimental data is proposed as an effective approach to approximate the elastic modulus of additively manufactured metals as a basis for predictable deformation under compressive loads with complex geometries such as the studied lattice structures.

Figure 4 illustrates the simulated force–displacement responses for various Young's modulus values across four lattice geometries: diamond, gyroid, BCC, and IWP. As expected, for a fixed elastic modulus, the force increases proportionally with increasing displacement, reflecting a linear elastic regime. The elastic modulus of the 3D-printed IN718 structures was estimated by matching simulation outputs with experimental compression data, as shown in Figure 5. Based on this comparison, the elastic modulus was approximated at around 10 GPa.

Our approach to estimating the Young's modulus involved conducting a parametric study that evaluated a wide range of elastic modulus values during simulations. This method allowed us to identify a value that most closely matched the experimental results from the compression tests. The significantly lower modulus compared to bulk IN718 (132 GPa according to Ghorbanpour et al. [38]) reflects the influence of microstructural features intrinsic to the SLM process, including porosity, residual stresses, and surface roughness. Using the estimated modulus enhances predictive capabilities across different lattice geometries, reducing experimental testing. This strategy streamlines the design process and diminishes costs related to prototyping, while also increasing the reliability of simulation models for future applications. In this way, our numerical models become effective tools for guiding the mechanical design of high-performance lattice structures tailored to specific application needs.

While the simulations predict proportional force responses consistent with the imposed displacements, the experimental force–displacement curves deviate from this ideal behavior. This discrepancy suggests that even at low strains, nonlinear deformation mechanisms may already be active in the printed structures.

Previous studies support the presence of complex mechanical responses in architected materials. For instance, Xu et al. [39] demonstrated that stress–strain curves for TPMS-based lattices exhibit three distinct stages: linear elastic, yielding, and densification. Similar trends have been observed in stereolithography (SLA)-printed lattice structures made from elastomeric materials, where a linear phase is more clearly defined at small displacements [34]. However, SLA typically produces smoother surfaces and fewer defects compared to metal additive manufacturing. In the case of SLM-fabricated IN718, the process involves high-energy laser exposure, which can introduce residual stresses, microcracks, and uneven surface textures during rapid solidification. These microstructural characteristics likely contribute to the early onset of nonlinear behavior in the printed structures, even within the nominally elastic regime.

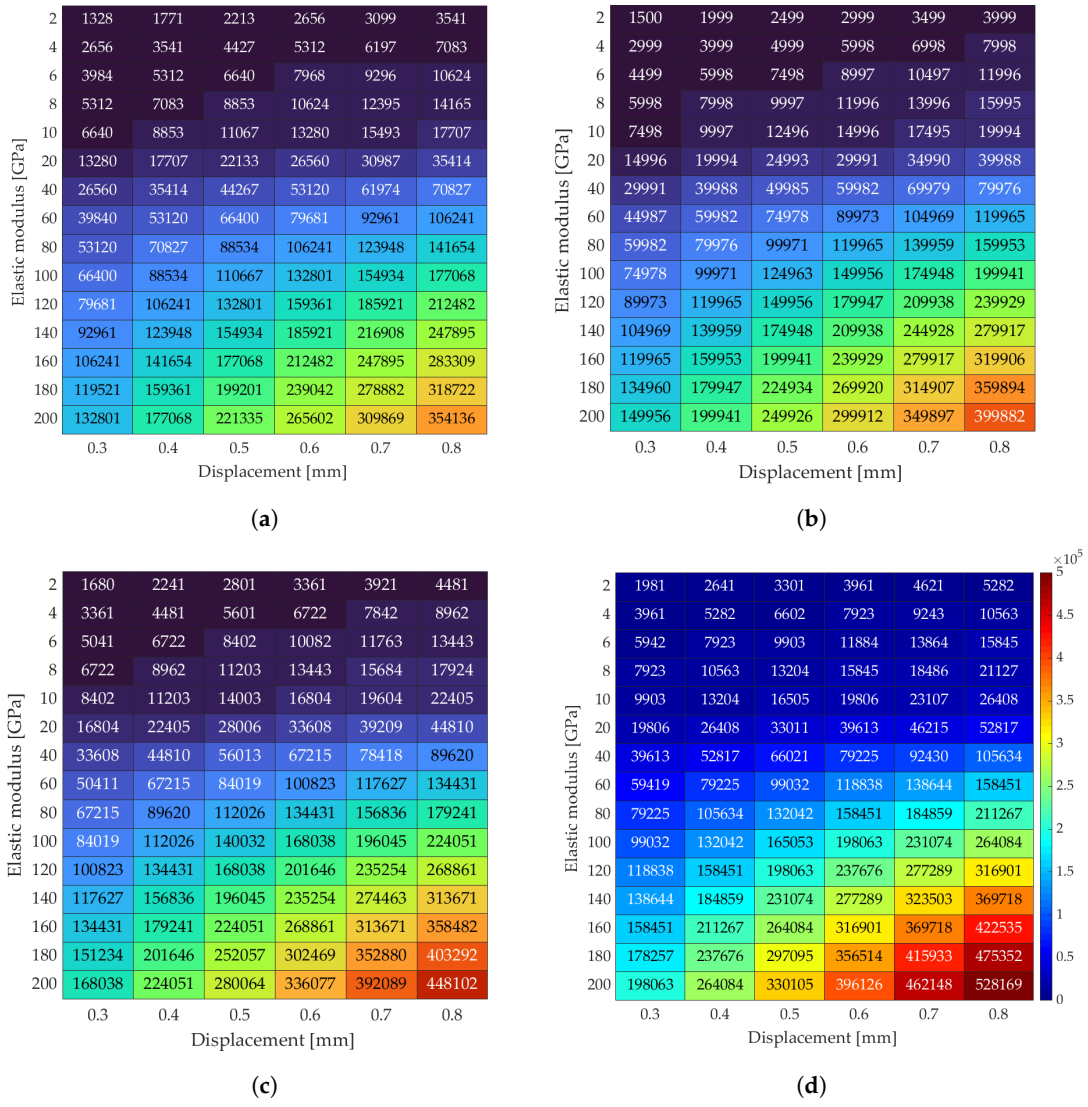


Figure 4. Reaction forces as a function of the simulated displacement and elastic modulus for all studied lattices (**a**) Diamond, (**b**) Gyroid, (**c**) BCC, and (**d**) IWP.

It is important to note that defects, while present, typically act as perturbations rather than fundamentally altering the overall material behavior. Thus, while discrepancies between experimental results and simulations may arise due to these microstructural variations, the primary mechanical response remains largely predictable within the linear range, affirming the validity of our simulation framework for assessing the performance of the lattice structures. This analysis complements the experimental findings by clarifying how stress propagates within each lattice structure under compressive loading. Such information is critical for evaluating the structural suitability of these architected materials in engineering applications and facilitates a more complete understanding of their mechanical behavior.

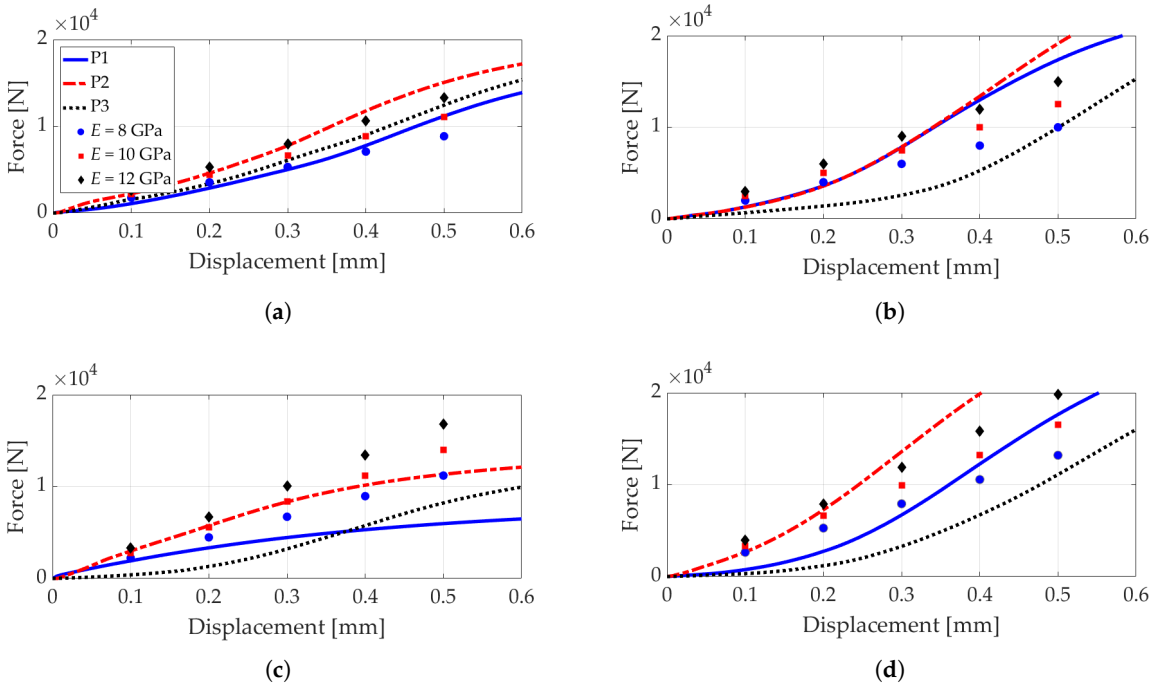


Figure 5. Simulation vs. experimental averaged (4 samples) force versus displacement for parameters 1, 2, 3. (**a**) Diamond, (**b**) Gyroid, (**c**) BCC, (**d**) IWP.

Further analyzing the mechanical behavior of the four studied lattice structures, an additional set of numerical simulations was conducted using the same STL files employed for their fabrication. A displacement of −0.8 mm was applied along the *z*-axis, with material properties defined by a Young's modulus of 10 GPa and a Poisson's ratio of 0.35. The results, presented in Figure 6, include von Mises stress plots that reveal distinct stress distribution patterns across the different lattice geometries. These patterns offer valuable insights into deformation behavior and highlight potential failure zones specific to each architecture.

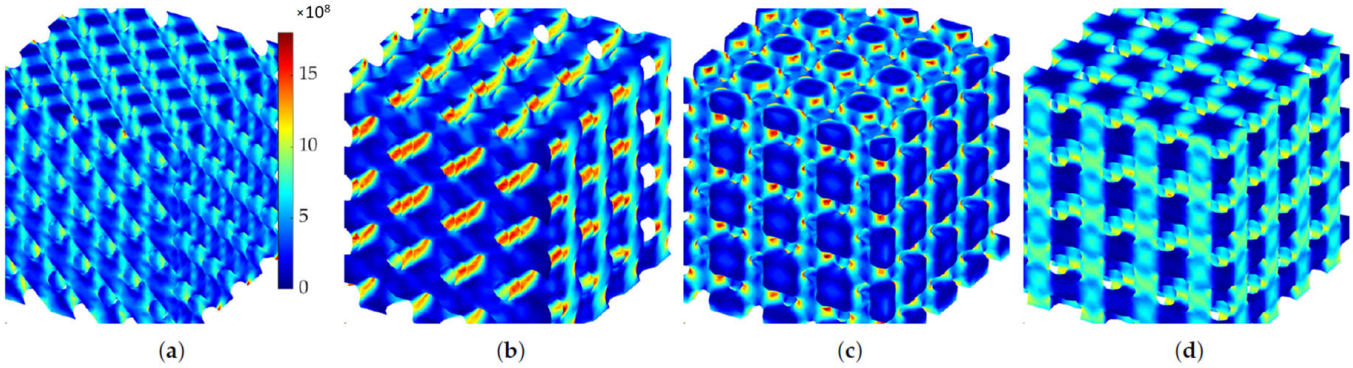


Figure 6. Von Mises stress while imposed a displacement is equal to −0.8 mm in z direction, a Young's modulus of 10 GPa, and a Poisson's ratio of 0.35. (**a**) Diamond (**b**) gyroid, (**c**) BCC, (**d**) IWP.

4. Experimental Results for Heat Treatments and Microstructural Characterization

4.1. Compression Test

The force–displacement curves presented in Figure 7a illustrate the relationship between the applied compressive force and the resulting displacement for various lattice geometries—diamond, gyroid, BCC, and IWP—fabricated with different sets of printing

parameters (P1, P2, and P3). The printing parameters, detailed in Table 3, were specifically adjusted for IN718 and systematically varied to investigate their influence on the mechanical properties of the lattice structures. The experimental data for compressive tests demonstrate that the P2 parameter set improved mechanical strength compared to parameter sets P1 and P3.

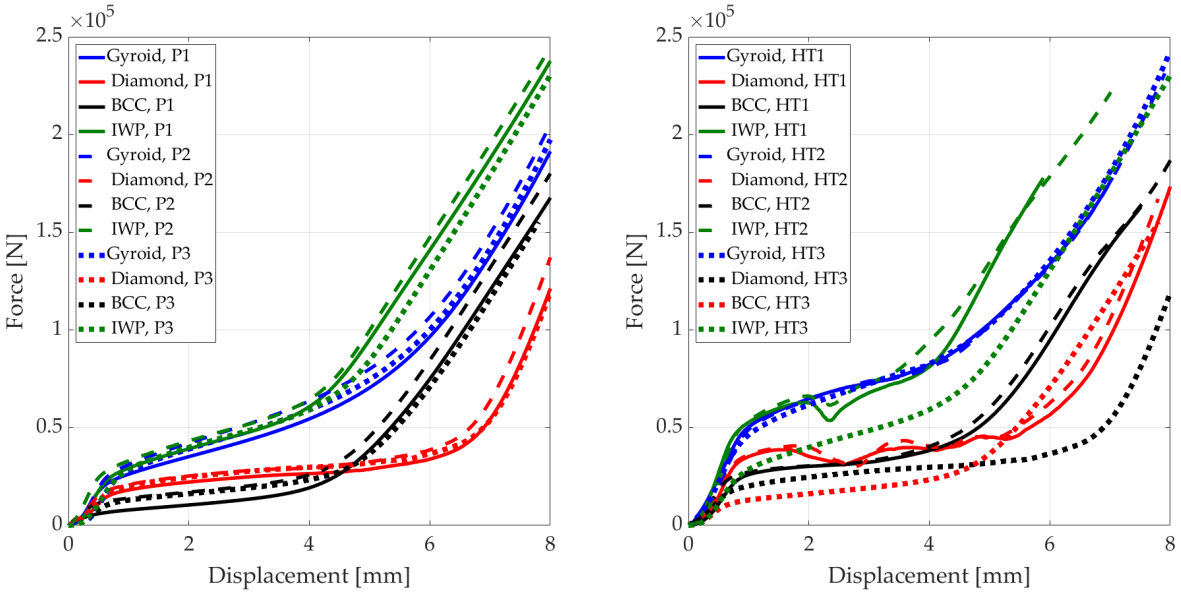


Figure 7. (**a**) Averaged (4 samples) force as a function of displacement for printing parameters set P1, P2, and P3. (**b**) Averaged (3 samples) force as a function of displacement for different heat treatments.

As noted in Table 1, the volume of the lattice structures decreases in order from IWP to gyroid, diamond, and then BCC. This means that the IWP lattice has the largest volume, followed by gyroid, diamond, and BCC. In the elastic region, the force required for a fixed displacement also decreases in the order of IWP, gyroid, diamond, and BCC. This indicates that the IWP lattice requires the highest force to achieve a given displacement, while the BCC lattice requires the lowest force. The relationship between the volume and the elastic force suggests that the lattice structures with larger volumes tend to have higher stiffness and require more force to achieve the same displacement in the elastic region. Conversely, the lattice structures with smaller volumes tend to be more compliant and require less force to deform.

The experimental results indicate that both lattice geometry and printing parameters significantly affect the compressive behavior. Distinct force–displacement responses were observed across the different parameter sets, demonstrating that stiffness and energy absorption can be tailored through controlled adjustment of printing conditions (see Figure 7a).

The results of the compression tests based on force–displacement curves revealed variations in the mechanical response among the different lattice topologies and heat treatment conditions. Specifically, the IWP HT1, Diamond HT1, and Diamond HT2 samples exhibited irregular profiles, with multiple force drops and intermittent load-bearing capacity, suggesting a combination of ductile and brittle failure modes. In contrast, the remaining samples showed smoother curves with a more gradual increase in force, indicative of predominantly ductile behavior. These trends suggest that heat treatment plays a key role in stabilizing the deformation mechanisms. Previous studies have demonstrated that lattice cell size significantly influences the mechanical performance and failure modes of architected structures

by governing the onset of buckling, plastic collapse, or brittle fracture under load [40]. A similar observation was reported by Cheloni et al. [41], who identified shear fracture and crushing as dominant failure modes in TPMS and BCC structures, further reinforcing the dependence of failure mechanisms on lattice topology and strut dimensions.

The variation in compressive performance and failure behavior across different geometries and parameter sets underscores the critical role of process parameter selection in achieving the desired mechanical performance for specific applications. These findings highlight the necessity of tuning printing parameters to improve structural resilience. Moreover, the integration of numerical simulations with experimental validation provides a comprehensive view of the mechanical response of these complex, lightweight structures, thereby supporting more informed design decisions in high-performance engineering applications.

The studied lattice geometries possess smooth, continuous surfaces that can efficiently distribute loads, making them particularly attractive for energy-absorbing and load-bearing applications in the aerospace and automotive sectors. Nonetheless, expanding the design scope in future work to include alternative multifunctional topologies (e.g., auxetic or biomimetic structures) would provide valuable insights into the mechanical behavior of additively manufactured lightweight structures, envisioned and ideal for different purposes.

Figure 7b presents the results of the compressive test for the lattice geometries subjected to three different heat treatment protocols (HT1, HT2, and HT3). The data demonstrate that both lattice geometry and thermal processing substantially influence the compressive response, highlighting its significant role in tailoring the mechanical properties of printed IN718 lattices.

The force–displacement curves reveal that HT1 and HT2 produced similar compressive behavior across all geometries, suggesting comparable microstructural outcomes. This similarity is likely due to analogous temperature profiles and holding times, which may have resulted in equivalent grain structures, precipitation behavior, and other metallurgical characteristics within the IN718 alloy.

In contrast, the HT3 condition led to a distinctly different mechanical response, indicating significant variations in microstructural evolution compared to HT1 and HT2. These differences could be attributed to enhanced precipitation hardening, altered grain size, or the formation of specific phases unique to the HT3 protocol.

The findings of this study align with previous work on the mechanical behavior of SLMed lattice structures. Yan et al. [1] highlighted the combined influence of geometry design and post-processing conditions on the performance of IN718 components, a phenomenon also evident in this research. Prior studies have likewise emphasized the critical role of heat treatment protocols in enhancing the mechanical response of SLM printed IN718 structures [5,17]. The improvements demonstrated in this study further support that carefully tailored heat treatment protocols can improve structural stability, refine microstructural characteristics, and enable the tuning of mechanical behavior in lattice architectures [15,16].

4.2. Microstructural Analysis

The X-ray diffraction (XRD) patterns obtained from the SLM IN718 samples subjected to heat treatments HT1, HT2, and HT3 reveal significant differences in phase constitution and crystallographic texture, as illustrated in Figure 8. All samples exhibit the characteristic peaks of the γ phase (face-centered cubic matrix), corresponding to the (111), (200), and (220) planes, which are consistent with those reported by Zhao et al. [42]. Interestingly, the (111) peak is more intense than the (200) peak in the HT2-treated sample, whereas the opposite trend is observed in HT1 and HT3. This behavior closely resembles the diffraction pattern of IN718 powder reported by Başcı et al. [43], where the (111) peak dominates. In

contrast, their heat-treated IN718 samples show a more pronounced (200) peak, indicating the development of a preferred crystallographic orientation. The stronger (111) reflection in HT2 suggests a more random and homogeneous grain orientation, likely resulting from enhanced phase dissolution and reprecipitation mechanisms during thermal treatment. Additionally, the (220) peak is also more pronounced in HT2, implying enhanced symmetry and improved lattice definition within the FCC matrix. Overall, this microstructural state is consistent with the improved mechanical behavior observed in HT2-treated specimens. A key distinction appears in the region between $2\theta \approx 37°$ and 43°, where small diffraction peaks are detected in HT1 and HT3 but are absent in HT2. These secondary peaks are typically associated with the presence of intergranular carbides (NbC), the brittle δ phase (Ni_3Nb), or coarsely precipitated γ'' (Ni_3Nb). Their detection in HT1 and HT3 indicates incomplete dissolution of segregated phases during solution treatment, consistent with the lower mechanical performance observed in these conditions. This suggests that Nb-rich phases such as Laves and δ formed during rapid solidification were not fully reabsorbed into the γ matrix, resulting in localized chemical inhomogeneities. Such microsegregation hinders uniform precipitation of γ' and γ'' phases, disrupts lattice coherency, and may promote intergranular weakening, all contributing to reduced mechanical integrity.

Conversely, the absence of peaks in this range in the HT2 pattern confirms the effective elimination of these secondary phases, as well as the possible presence of finely dispersed and coherent γ'' precipitates that do not contribute significantly to diffraction intensity. Liu et al. [44] reported that solution treatment at 1060 °C effectively dissolved Laves phases, facilitating the uniform precipitation of γ' and γ'', supporting the observations made for the HT2-treated samples.

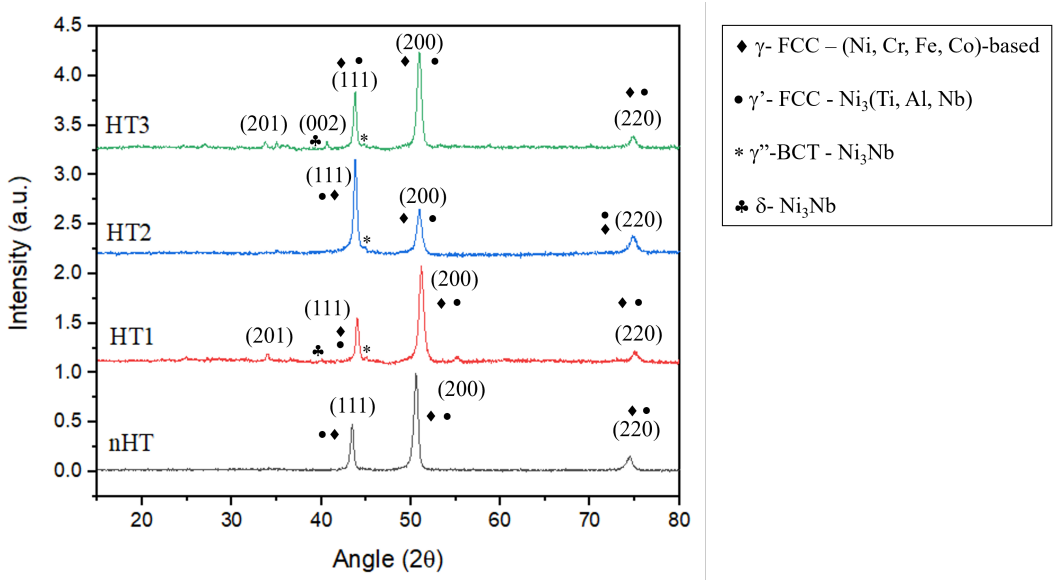


Figure 8. Non- and heat-treated IWP samples XRD. The peaks corresponding to the γ matrix, γ'' phase, γ' phase, and δ phase are indicated.

Optical microscopy and X-ray diffraction (XRD) analyses revealed that heat treatment conditions significantly influenced the microstructure features of the printed specimens. Samples subjected to HT2 exhibited larger grain sizes and well-defined γ' and γ'' phases, which correlate with enhanced mechanical performance, as reported in previous studies [18,19]. These microstructural distinctions are illustrated in Figure 9.

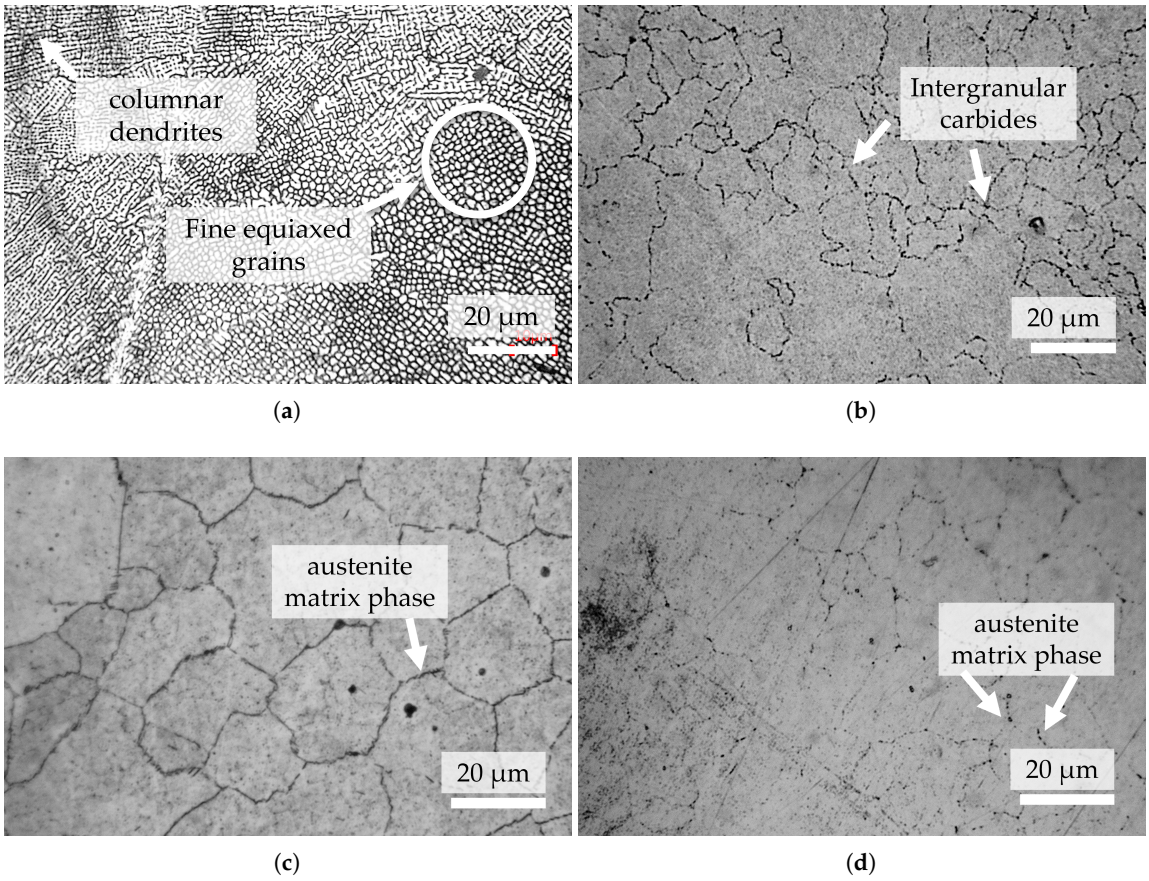


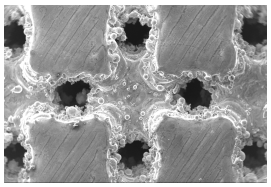
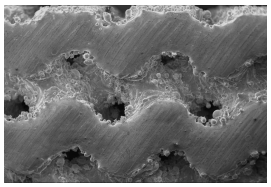
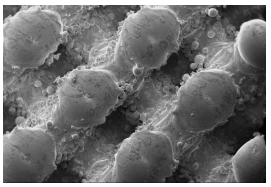
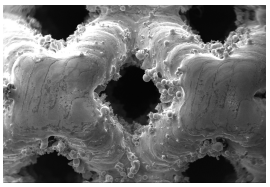
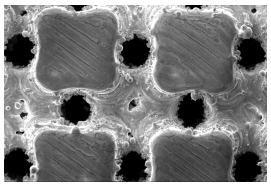
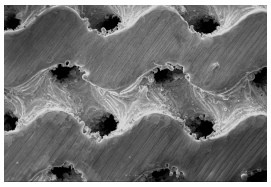
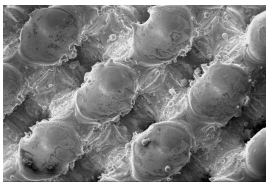
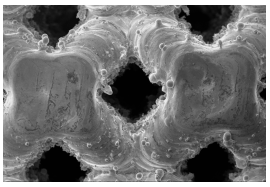
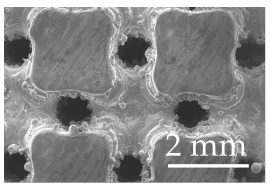
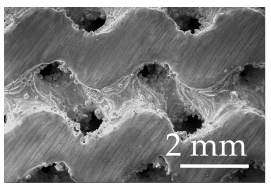
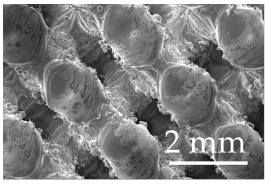
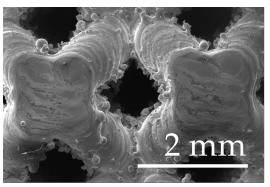
Figure 9. Microstructural analysis of the SLM IN718 subjected to different heat treatments. (**a**) As-built sample (nHT), (**b**) HT1, (**c**) HT2, and (**d**) HT3.

Among the evaluated conditions, HT2 produced the most homogeneous and refined microstructure, characterized by a pronounced presence of strengthening γ' and γ'' phases. This microstructural refinement indicates the efficacy of HT2 in promoting phase stability and precipitation hardening, thereby contributing to superior mechanical properties.

To further investigate microstructural features, scanning electron microscopy (SEM) was employed, providing high-resolution imaging of grain boundaries, phase distributions, and defect morphology. The SEM analysis confirmed that HT2-treated samples exhibited fewer defects and a more uniform microstructure compared to those treated with HT1 and HT3, supporting the observed improvements in mechanical behavior [17].

Table 4 presents SEM images comparing pore integrity across different lattice geometries processed under three parameter sets: (P1) $P = 300$ W, $v = 900$ mm/s; (P2) $P = 300$ W, $v = 1000$ mm/s; and (P3) $P = 200$ W, $v = 525$ mm/s. The second parameter set demonstrated superior structural integrity across all geometries, as evidenced by reduced pore formation and fewer satellite particles, indicating improved powder fusion during the selective laser melting process. This suggests that, in addition to heat treatment, appropriate selection of processing parameters plays a pivotal role in minimizing defects and enhancing the overall quality of lattice structures. In fact, Estrada-Diaz et al. [25,28] have noted that the resulting properties of SLM-printed components, including densification and mechanical properties, is driven by the interaction between process parameters and material properties.Though small discrepancies in the observed results may arise from subtle variations in the specific characteristic of different material batches, the mechanisms governing, for instance structural integrity of SLMed components, remain.

Table 4. SEM images of manufactured samples.

Parameter	I-WP	Gyroid	Diamond	BCC
P = 300 W, v = 900 mm/s				
P = 300 W, v = 1000 mm/s				
P = 200 W, v = 525 mm/s				

The role of heat treatments in promoting the formation of γ' and γ'' phases was further confirmed through differential scanning calorimetry (DSC) analysis. The DSC analysis (data not included) revealed distinct exothermic peaks corresponding to the precipitation of these phases in HT2-treated samples, demonstrating the effectiveness of this tailored heat treatment in enhancing mechanical strength. These results align with previous studies highlighting the critical contribution of γ' and γ'' phases to improved mechanical performance in IN718.

Additionally, microstructural evaluation revealed a clear influence of post-processing heat treatments on intergranular carbide formation and its effect on compressive behavior. Samples treated with HT1 and HT3 exhibited significant carbide precipitation along grain boundaries, indicating incomplete dissolution during solution treatment or cooling stages. This intergranular carbide distribution can serve as preferential sites for microcrack nucleation under compressive loading, reducing grain boundary cohesion and promoting brittle failure mechanisms. In contrast, HT2-treated samples showed no visible intergranular carbides, likely due to a more suitable combination of holding time and temperature that enabled complete carbide dissolution, overcoming issues associated with rapid solidification in SLM processes. This homogeneous microstructure correlates with superior compressive performance, as HT2 consistently exhibited the highest mechanical strength.

While the microstructural and phase analyses conducted via SEM and XRD align well with the mechanical results, further quantitative characterization, such as pore size distribution and phase fraction analysis, could strengthen the understanding of the relationship between microstructure and mechanical performance.

Overall, this comprehensive microstructural analysis confirms that a carefully tailored heat treatment schedule not only governs the morphology and distribution of secondary phases, such as γ'/γ'' precipitates and carbides, but also significantly enhances the mechanical properties of SLM-fabricated IN718 lattice structures. By tuning heat treatment parameters, it is possible to achieve a balanced combination of strength, ductility, and toughness, enabling the deployment of these architected materials in high-performance applications across demanding environments.

5. Conclusions

This study investigated the influence of printing parameters, lattice geometry, and tailored heat treatments on the mechanical performance of Inconel 718 lattice structures fabricated via SLM. Through experimental compression testing, microstructural analysis, and numerical simulation, critical insights were gained into how manufacturing and post-processing conditions affect compressive strength, stiffness, and energy absorption.

The main findings are summarized as follows:

- Tailored heat treatments significantly enhanced mechanical performance, with the HT3 protocol increasing yield strength by approximately 25% and energy absorption capacity by 30% compared to HT1 and HT2. These improvements were attributed to a refined microstructure, characterized by uniform γ'/γ'' phase distribution and the elimination of intergranular carbides.
- Lattice geometry and printing parameters directly influenced compressive behavior, with adjustments in laser power, scan speed, hatch spacing, and layer thickness resulting in variations of up to 20% in stiffness across different parameter sets. The parameter set 2 ($P = 300$ W, $v = 1000$ mm/s) demonstrated superior structural integrity, as evidenced by reduced porosity and improved powder fusion observed in SEM analyses.
- Numerical simulations accurately predicted the linear elastic response of the diamond, gyroid, and IWP geometries, showing deviations of less than 5% from experimental force–displacement curves for displacements up to 0.8 mm. For the BCC geometry, nonlinear effects emerged beyond 0.3 mm, leading to increased discrepancies between the simulation and experimental data.
- Microstructural analyses confirmed the critical role of heat treatment tuning, with HT2 and HT3 treatments reducing defect density by approximately 40% compared to untreated or sub-optimally treated samples, thereby enhancing mechanical reliability under compressive loading.

These findings advance the understanding of process-structure-property relationships in SLM-fabricated Inconel 718 lattice structures and demonstrate the potential of tailored heat treatments and printing strategies to achieve high-performance, lightweight components.

Future work will focus on developing advanced mathematical models that incorporate nonlinear deformation behavior, microstructural evolution, and defect characterization to more accurately predict mechanical performance. Such predictive tools will facilitate the design and industrial deployment of architected materials tuned for aerospace, automotive, and energy absorption applications. Moreover, implementing artificial intelligence approaches, such as physics-informed neural networks and meta-heuristic methodologies, offers the capability for the simultaneous and agile enhancement of properties of interest in lightweight IN718 structures, including fatigue life, energy dissipation, and heat transfer. Likewise, the incorporation of additional surface treatments such as shot peening could lead to a further enhanced performance.

Author Contributions: Conceptualization, R.G.-N. and O.M.-R.; methodology, M.J.B.-M., P.M., and R.G.-N.; software, P.M. and J.A.E.-D.; validation, R.G.-N., D.O.-T., and O.M.-R.; formal analysis, M.J.B.-M., R.G.-N., P.M., and J.A.E.-D.; investigation, M.J.B.-M., R.G.-N., and P.M.; resources, A.E.-Z., D.O.-T., O.M.-R., and I.A.P.-M.; data curation, R.G.-N., J.A.E.-D., and O.M.-R.; writing—original draft preparation, M.J.B.-M., R.G.-N., P.M., and D.O.-T.; writing—review and editing, R.G.-N., P.M., J.A.E.-D., A.E.-Z., D.O.-T., O.M.-R., and I.A.P.-M.; visualization, M.J.B.-M., R.G.-N., P.M., and D.O.-T.; supervision, A.E.-Z., D.O.-T., and O.M.-R.; project administration, O.M.-R., D.O.-T., and I.A.P.-M.;

funding acquisition, A.E.-Z., D.O.-T., O.M.-R., and I.A.P.-M. All authors have read and agreed to the published version of the manuscript.

Funding: This research was funded by Tecnologico de Monterrey project entitled "Smart Lightweighting: Developing Biodegradable Polymers with Programmable Degradation for Advanced 3D Printing in Engineering and Biomedical Applications", Project ID: JXT070-23EG60001, from Challenge-Based Research Funding Program 2023, Tecnologico de Monterrey.

Data Availability Statement: Data generated or analyzed during this study are available from the corresponding author upon reasonable request. Data are available under certain conditions.

Acknowledgments: The characterizations were performed in the National Laboratory in Additive Manufacturing, 3D Digitizing and Computed Tomography (MADiT).

Conflicts of Interest: The authors declare no conflicts of interest.

References

1. Yan, C.; Hao, L.; Hussein, A.; Raymont, D. Evaluations of cellular lattice structures manufactured using selective laser melting. *Int. J. Mach. Tools Manuf.* **2012**, *62*, 32–38. [CrossRef]
2. Mazur, M.; Leary, M.; McMillan, M.; Sun, S.; Shidid, D.; Brandt, M. 5—Mechanical properties of Ti6Al4V and AlSi12Mg lattice structures manufactured by Selective Laser Melting (SLM). In *Laser Additive Manufacturing*; Brandt, M., Ed.; Woodhead Publishing Series in Electronic and Optical Materials; Woodhead Publishing: Cambridge, UK, 2017; pp. 119–161. [CrossRef]
3. Feng, Q.; Tang, Q.; Liu, Z.; Liu, Y.; Setchi, R. An investigation of the mechanical properties of metallic lattice structures fabricated using selective laser melting. *Proc. Inst. Mech. Eng. Part J. Eng. Manuf.* **2018**, *232*, 1719–1730. [CrossRef]
4. Sing, S.L.; Wiria, F.E.; Yeong, W.Y. Selective laser melting of lattice structures: A statistical approach to manufacturability and mechanical behavior. *Robot. Comput.-Integr. Manuf.* **2018**, *49*, 170–180. [CrossRef]
5. Yang, P.; Su, H.; Guo, Y.; Zhou, H.; Xia, L.; Shen, Z.; Wang, M.; Zhang, Z.; Guo, M. Influence of cooling rate during the heat treatment process on the precipitates and ductility behavior of inconel 718 superalloy fabricated by selective laser melting. *Mater. Sci. Eng. A* **2024**, *902*, 146603. [CrossRef]
6. Zhang, Y.; Yang, L.; Lu, W.; Wei, D.; Meng, T.; Gao, S. Microstructure and elevated temperature mechanical properties of IN718 alloy fabricated by laser metal deposition. *Mater. Sci. Eng. A* **2020**, *771*, 138580. [CrossRef]
7. Huang, Y.; Wang, T.; Liu, L.; Li, Y.; Han, C.; Tan, H.; Zhou, W.; Yang, Y.; Wang, D. Thermomechanical Behavior and Experimental Study of Additive Manufactured Superalloy/Titanium Alloy Horizontal Multi-Material Structures. *Metals* **2025**, *15*, 454. [CrossRef]
8. Zaharia, S.M.; Lancea, C.; Kruk, A.; Cempura, G.; Gruszczyński, A.; Chicos, L.A.; Pop, M.A. Mechanical Properties and Microstructure of Inconel 718 Lattice Structures Produced by Selective Laser Melting Process. *Materials* **2024**, *17*, 622. [CrossRef]
9. Banait, S.; Jin, X.; Campos, M.; Pérez-Prado, M. Precipitation-induced transition in the mechanical behavior of 3D printed Inconel 718 bcc lattices. *Scr. Mater.* **2021**, *203*, 114075. [CrossRef]
10. Wang, X.; Wang, C.; Zhou, X.; Wang, D.; Zhang, M.; Gao, Y.; Wang, L.; Zhang, P. Evaluating Lattice Mechanical Properties for Lightweight Heat-Resistant Load-Bearing Structure Design. *Materials* **2020**, *13*, 4786. [CrossRef]
11. Thuneman, T.; Raja, K.S.; Charit, I. Room Temperature Corrosion Behavior of Selective Laser Melting (SLM)-Processed Ni-Fe Superalloy (Inconel 718) in 3.5% NaCl Solution at Different pH Conditions: Role of Microstructures. *Crystals* **2024**, *14*, 89. [CrossRef]
12. Bai, L.; Gong, C.; Chen, X.; Sun, Y.; Xin, L.; Pu, H.; Peng, Y.; Luo, J. Mechanical properties and energy absorption capabilities of functionally graded lattice structures: Experiments and simulations. *Int. J. Mech. Sci.* **2020**, *182*, 105735. [CrossRef]
13. Ozdemir, Z.; Hernandez-Nava, E.; Tyas, A.; Warren, J.A.; Fay, S.D.; Goodall, R.; Todd, I.; Askes, H. Energy absorption in lattice structures in dynamics: Experiments. *Int. J. Impact Eng.* **2016**, *89*, 49–61. [CrossRef]
14. Choi, K.H.; Shin, G.Y.; Lee, K.Y.; Shim, D.S. Directed Energy Deposition on Structurally Low-density Substrate and its Effects on Microstructural and Interfacial Bonding Characteristics. *Int. J. Precis. Eng.-Manuf.-Green Technol.* **2024** . [CrossRef]
15. Zhang, M.; Yang, Y.; Wang, D.; Xiao, Z.; Song, C.; Weng, C. Effect of heat treatment on the microstructure and mechanical properties of Ti6Al4V gradient structures manufactured by selective laser melting. *Mater. Sci. Eng. A* **2018**, *736*, 288–297. [CrossRef]
16. Li, D.; Qin, R.; Xu, J.; Chen, B.; Niu, X. Effect of heat treatment on AlSi10Mg lattice structure manufactured by selective laser melting: Microstructure evolution and compression properties. *Mater. Charact.* **2022**, *187*, 111882. [CrossRef]
17. Wang, W.; Chen, Z.; Lu, W.; Meng, F.; Zhao, T. Heat treatment for selective laser melting of Inconel 718 alloy with simultaneously enhanced tensile strength and fatigue properties. *J. Alloys Compd.* **2022**, *913*, 165171. [CrossRef]

18. Huang, L.; Cao, Y.; Zhang, J.; Gao, X.; Li, G.; Wang, Y. Effect of heat treatment on the microstructure evolution and mechanical behaviour of a selective laser melted Inconel 718 alloy. *J. Alloys Compd.* **2021**, *865*, 158613. [CrossRef]
19. Schneider, J.; Lund, B.; Fullen, M. Effect of heat treatment variations on the mechanical properties of Inconel 718 selective laser melted specimens. *Addit. Manuf.* **2018**, *21*, 248–254. [CrossRef]
20. Zhang, X.; Wang, S.; Liu, H.; Liang, Y.; Yi, F.; Lin, J. Microstructure evolution and mechanical properties of additively manufactured Ni-based GH4099 superalloy via hot isostatic pressing and heat treatment. *Mater. Sci. Eng. A* **2024**, *903*, 146696. [CrossRef]
21. Ma, K.; Wang, J. Microstructural Characteristics and Mechanical Properties of an Additively Manufactured Nickel-Based Superalloy. *Crystals* **2022**, *12*, 1358. [CrossRef]
22. Yu, S.; Sun, J.; Bai, J. Investigation of functionally graded TPMS structures fabricated by additive manufacturing. *Mater. Des.* **2019**, *182*, 108021. [CrossRef]
23. Al-Ketan, O.; Rowshan, R.; Abu Al-Rub, R.K. Topology-mechanical property relationship of 3D printed strut, skeletal, and sheet based periodic metallic cellular materials. *Addit. Manuf.* **2018**, *19*, 167–183. [CrossRef]
24. Baskaran, J.; Muthukannan, D.; Shukla, R.; Konda Gokuldoss, P. Manufacturability and deformation studies on a novel metallic lattice structure fabricated by Selective Laser Melting. *Vacuum* **2024**, *222*, 113065. [CrossRef]
25. Estrada-Díaz, J.A.; Elías-Zúñiga, A.; Martínez-Romero, O.; Olvera-Trejo, D. Enhanced Mathematical Model for Producing Highly Dense Metallic Components through Selective Laser Melting. *Materials* **2021**, *14*, 1571. [CrossRef]
26. Estrada-Díaz, J.A.; Elías-Zúñiga, A.; Martínez-Romero, O.; Palacios-Pineda, L.M.; Guzmán-Nogales, R.; Cedeño-Viveros, L.D.; Olvera-Trejo, D. A novel mathematical model for predicting a sustainable selective laser melting and controlled densification. *Int. J. Sustain. Eng.* **2024**, *17*, 239–249. [CrossRef]
27. Rosete, D.X. Validation of the Process Parameter for Enhancing Densification and Thermal Conductivity of the IN718 superalloy manufactured by Selective Laser Melting. Master's Thesis, Tecnologico de Monterrey, Monterrey, Mexico, 2022.
28. Estrada-Díaz, J.A.; Elías-Zúñiga, A.; Martínez-Romero, O.; Rodríguez-Salinas, J.; Olvera-Trejo, D. A Mathematical Dimensional Model for Predicting Bulk Density of Inconel 718 Parts Produced by Selective Laser Melting. *Materials* **2021**, *14*, 512. [CrossRef]
29. Ghiaasiaan, R.; Poudel, A.; Ahmad, N.; Muhammad, M.; Gradl, P.R.; Shao, S.; Shamsaei, N. Room Temperature Mechanical Properties of Additively Manufactured Ni-base Superalloys: A Comparative Study. *Procedia Struct. Integr.* **2022**, *38*, 109–115. [CrossRef]
30. *ISO 13314*; Mechanical Testing of Metals—Ductility Testing—Compression Test for Porous and Cellular Metals. International Organization for Standardization (ISO): Geneva, Switzerland, 2011.
31. Song, J.; Zhang, L.; Wu, W.; He, B.; Ni, X.; Xu, J.; Zhu, G.; Yang, Q.; Wang, T.; Lu, L. Understanding processing parameters affecting residual stress in selective laser melting of Inconel 718 through numerical modeling. *J. Mater. Res.* **2019**, *34*, 1395–1404. [CrossRef]
32. Lu, Y.; Wu, S.; Gan, Y.; Huang, T.; Yang, C.; Junjie, L.; Lin, J. Study on the microstructure, mechanical property and residual stress of SLM Inconel-718 alloy manufactured by differing island scanning strategy. *Opt. Laser Technol.* **2015**, *75*, 197–206. [CrossRef]
33. Estrada -Diaz, J.A.; Martinez-Romero, O.; Olvera-Trejo, D.; Elias-Zuniga, A. Elucidating the Fractal Nature of Powder Bed in Selective Laser Melting of Metallic Components. *Fractals* **2022**, *30* . [CrossRef]
34. Majari, P.; Olvera-Trejo, D.; Estrada-Díaz, J.A.; Elías-Zúñiga, A.; Martinez-Romero, O.; Ramírez-Herrera, C.A.; Perales-Martínez, I.A. Enhanced Lightweight Structures Through Brachistochrone-Inspired Lattice Design. *Polymers* **2025**, *17*, 654. [CrossRef] [PubMed]
35. Ibrahim, Y.; Li, Z.; Davies, C.; Maharaj, C.; Dear, J.; Hooper, P. Acoustic resonance testing of additive manufactured lattice structures. *Addit. Manuf.* **2018**, *24*, 566–576. [CrossRef]
36. Mahshid, R.; Hansen, H.N.; Højbjerre, K.L. Strength analysis and modeling of cellular lattice structures manufactured using selective laser melting for tooling applications. *Mater. Des.* **2016**, *104*, 276–283. [CrossRef]
37. Mazur, M.; Leary, M.; Sun, S.; Vcelka, M.; Shidid, D.; Brandt, M. Deformation and failure behaviour of Ti-6Al-4V lattice structures manufactured by selective laser melting (SLM). *Int. J. Adv. Manuf. Technol.* **2016**, *84*, 1391–1411. [CrossRef]
38. Ghorbanpour, S.; Deshmukh, K.; Sahu, S.; Riemslag, T.; Reinton, E.; Borisov, E.; Popovich, A.; Bertolo, V.; Jiang, Q.; Sanchez, M.; et al. Additive manufacturing of functionally graded inconel 718: Effect of heat treatment and building orientation on microstructure and fatigue behaviour. *J. Mater. Process. Technol.* **2022**, *306*, 117573. [CrossRef]
39. Xu, K.; Cao, J.; Zheng, Z.; Zhao, R.; Xu, G.; Wang, H.; Wang, J.; Hur, B.; Yue, X. Deformation Behavior of Inconel 625 Alloy with TPMS Structure. *Materials* **2025**, *18*, 396. [CrossRef]
40. Maskery, I.; Aboulkhair, N.; Aremu, A.; Tuck, C.; Ashcroft, I. Compressive failure modes and energy absorption in additively manufactured double gyroid lattices. *Addit. Manuf.* **2017**, *16*, 24–29. [CrossRef]
41. Cheloni, J.P.M.; Zluhan, B.; Silveira, M.E.; Fonseca, E.B.; Valim, D.B.; Lopes, E.S. Mechanical behavior and failure mode of body-centered cubic, gyroid, diamond, and Voronoi functionally graded additively manufactured biomedical lattice structures. *J. Mech. Behav. Biomed. Mater.* **2025**, *163*, 106796. [CrossRef]

42. Zhao, X.; Zhao, X.; Xu, Y.; Shi, Y. Friction Performance Analysis of WC-Reinforced IN718 Composite Material Based on SLM Process. *Metals* **2024**, *14*, 1361. [CrossRef]
43. Başçı, Ü.G.; Avcu, E.; Kıraç, M.; Sever, A.; Gökalp, İ.; Yavuz, H.İ.; Oktay, S.; Abakay, E.; Yıldıran Avcu, Y.; Yamanoğlu, R. Microstructural, Mechanical, and Tribological Properties of Selective Laser Melted Inconel 718 Alloy: The Influences of Heat Treatment. *Crystals* **2025**, *15*, 18. [CrossRef]
44. Liu, X.; Wang, T.; Li, N.; Wei, L.; Jiang, S. Effects of heat treatments on the microstructure and mechanical properties of Inconel 718 alloy fabricated by electron beam freeform fabrication. *Mater. Sci. Eng. A* **2024**, *908*, 146800. [CrossRef]

Disclaimer/Publisher's Note: The statements, opinions and data contained in all publications are solely those of the individual author(s) and contributor(s) and not of MDPI and/or the editor(s). MDPI and/or the editor(s) disclaim responsibility for any injury to people or property resulting from any ideas, methods, instructions or products referred to in the content.